Front. Earth Sci. 2022, 16(2): 236–247
https://doi.org/10.1007/s11707-021-0870-4

RESEARCH ARTICLE

The scattering mechanism of squall lines with C-Band dual polarization radar. Part II: the mechanism of an abnormal Z_{DR} echo in clear air based on the parameterization of turbulence deformation

Jiashan ZHU, Ming WEI (✉), Sinan GAO, Chunsong LU

Collaborative Innovation Center on Forecast and Evaluation of Meteorological Disasters, Nanjing University of Information Science & Technology, Nanjing 210044, China

Abstract In part I, the clear air echo in front of the squall line is caused by turbulence diffraction, which makes the Z_{DR} echo characteristics different from particle scattering. To study the turbulence deformation phenomenon that is affected by environmental wind, the turbulence-related method is used to analyze the characteristics of three-dimensional turbulence energy spectrum density, and the parametric model of turbulence integral length scale and environmental wind speed is established. The results show that the horizontal scale of turbulence is generally larger than the vertical scale. The turbulence is nearly isotropic in the horizontal direction, presenting a flat ellipsoid with the vertical orientation of the rotation axis when there is no horizontal wind or the horizontal velocity is small. When horizontal wind exists, the turbulence scale increases along the dominant wind direction. The turbulence scale is positively correlated with the wind speed. The power function is used to fit the relationships of turbulence integral length scale and horizontal wind speed, which obtains the best fitting effect, and the goodness of fit (GF) is above 0.99 in each direction. The deforming turbulence can cause 8–9 dB Z_{DR} anomalies in the echo of dual polarization radar, which the ratio of scales in the dominant wind and the vertical direction of deforming turbulence (L_u/L_w) is around 4.3. The variation in Z_{DR} depends on the turbulence shape, orientation and the relative position between turbulence and radar. The shape of turbulence derived from radar detection results is consistent with that of the parametric model, which can provide a parametric scheme for turbulence research. The results reveal the mechanism of abnormal Z_{DR} echo caused by deforming turbulence.

Received August 18, 2020; accepted January 5, 2021

E-mail: wm_nuist@126.com

Keywords dual polarization radar, clear air echo, Bragg diffraction, deforming turbulence, parameterization

1 Introduction

With the popularization of dual polarization Doppler weather radar, the radar not only plays an important role in detecting precipitation but also observes many clear air echo phenomena. In part I, the clear air echo in front of the squall line is caused by turbulence diffraction (or Bragg diffraction). Turbulence diffraction has been widely studied in previous decades (Melnikov et al., 2013; Richardson et al., 2017). The turbulence scale increases as the height increases. In the low troposphere, the minimum turbulence scale is about centimeter scale. In the tropopause, the minimum turbulence scale can be in the order of decimeters (Ma, 1986). Turbulence is common in atmospheric boundary layer, but the clear air echo caused by turbulence can only be detected by radar within a certain range. This phenomenon can be explained by Bragg Law and the theory of half wavelength (Bragg, 1913). Tatarski et al. (1961) developed the theory of electromagnetic scattering and deduced the formula for the scattering of electromagnetic waves in a turbulent medium. The experimental results verified that the turbulent scale that could produce a “diffraction bright spot” on the back scattering direction should be an integer times the radar wavelength. In other words, the minimum turbulence scale detected by radar is half of the wavelength. Bragg diffraction theory is used to analyze the cause of most clear air echoes (Doviak et al. 1994; Knight and Miller, 1993). Bragg diffraction echoes are also obvious in the polarization parameters. Huang et al. (2018) discussed the wind, temperature, humidity structure and dual

polarization parameters of the clear air echo and pointed out that the turbulence would be deformed by wind, which means that the Z_{DR} would be affected by the Doppler effect and result in an abnormal Z_{DR} echo in clear air.

Kolmogorov (1941a) first proposed the cascade theory of turbulence energy and analyzed the distribution characteristics of turbulence energy from the perspective of turbulence scale. Monin and Obukhov (1954) proposed the M-O similarity theory, gave the M-O characteristic length (L), discussed the influence of Reynolds stress and buoyancy on boundary layer turbulence energy transport, and established the general expression of boundary layer meteorological quantity profiles. Businger et al. (1971) established the Businger-Dyer similarity relationship, making the study of boundary layer turbulence more mature. The similarity theory can also be extended to the discussion of boundary layer turbulence statistics and turbulence spectrum rules, which is the theoretical basis of modern atmospheric turbulence research (Sheng et al., 2003). In addition, the study of large eddy simulation (LES) also provided a clear picture of turbulent organized structures (TOS). The spoke-like pattern consisted of two parts: one part included the networks of narrow thermal lines where individual thermals frequently arose, and the other part included wider circular regions surrounded by the thermal lines where downdrafts were dominant and thermal activities were not so active (Kanda et al., 2004). Wang et al. (2007 and 2009) used the global flux observatory network (FLUXNET), a method related to turbulence and the micrometeorology principle to measure the high-frequency turbulent pulsations of physical quantities. They calculated the covariance between the speed pulsation of vertical wind and pulsations of other physical quantities to obtain turbulent exchange and turbulence statistical quantities.

Although the theoretical study of boundary layer turbulence has been relatively mature, there are still few studies on its shape characteristics, especially on the deformation of turbulence under the influence of environmental wind. To discuss the relationship between turbulence and Z_{DR}, a parameterized model of turbulence shape is established based on the turbulence-related method, and the relationship between the abnormal Z_{DR} echo and deforming turbulence is analyzed in this study.

2 Data sets and methods

2.1 Data sets

Dual polarization weather radar data of a gust front were obtained on July 31, 2014 by the C-Band Dual Polarization Full Coherent Pulse Doppler Weather Radar at Nanjing University of Information Science & Technology (NUIST CDP radar). The time used in this paper is Beijing Time.

The observation data related to turbulence are obtained from the three-dimensional ultrasonic anemometer CSAT3 produced by Campbell. The data collector is CR5000, and the sampling frequency is 10 Hz. The observation site is located in Zhanjiang, Guangdong Province, China. The terrain around the observation site is flat. The probe of the turbulence measuring instrument is 1 m height above the ground. Turbulence data from March 13, 2017 are selected for analysis.

It may be noted that the radar data and turbulence data used in this paper is mismatched in time and place. Primarily in view of the probe of CSAT3 is 1 m height above the ground. However, the height of weather radar is usually located at an altitude more than 50 m above the ground. The elevation of radar is positive and there is beam broadening. In part I, the location of the abnormal Z_{DR} echoes is 30 km away from the radar, where the space of radar sampling is about 800 m above the ground. The actual sampling space detected by radar cannot coincide with the sampling space of CSAT3. So the two data sets cannot match each other in space. Therefore, we decide to use the turbulence data to establish a parameterized model of the extent of turbulence deformation and the environmental wind speed, and extrapolate the model to discuss the theoretical shape parameters of deforming turbulence and the parameters detected by radar. So the two data sets do not need to match each other in time.

2.2 Data preprocessing

The radar data used in this paper have been subjected to clutter filtering, attenuation correction and other quality control. The quality control of Φ_{DP} data are carried out by the method of Φ_{DP} data classification and processing proposed by Du et al. (2012). The K_{DP} data are fitted afresh by the adaptive variable distance least squares fitting method of Wang and Chandrasekar (2009). The attenuation correction of Z and Z_{DR} is performed using the Z_H-K_{DP} combined method by Hu et al. (2008). Besides, the algorithm of clear air echo data quality control generally adopted by Huang et al. (2018), Tang (2014) and Yao (2016) is used for quality control to obtain high quality clear air radar data.

The observation data of CSAT3 are preprocessed and quality controlled. The test method of variance (Vickers and Mahrt, 1997) is used to remove the observation outlier after the flag of the abnormal signal is eliminated. The multiple value of variance is generally between 3 and 6 (Guo et al., 2007). In this study, 5 times variance is used as the test standard. An important hypothesis of measuring the surface flux by a turbulence instrument is that the average vertical velocity in a period is 0. Therefore, the original wind data should be coordinate rotated, making the gradient direction normal, and the average scalar in the local area is in the u-w plane. The w axis is perpendicular to the local ground after coordinate rotation, and the average w is 0. Common methods of coordinate rotation include

double rotation (DR), triple rotation (TR), planar fit (PF), and others (Wilczak et al., 2001; Xu et al., 2008).

To discuss the deformation of turbulence, the DR method is referenced to address natural coordinates in this study. First, the vertical rotation correction is made to rotate the u-w plane around the v axis:

$$\begin{cases} \alpha = \arctan(\overline{w}_m/\overline{u}_m) \\ u = u_m\cos\alpha + w_m\sin\alpha \\ v = v_m \\ w = -u_m\sin\alpha + w_m\cos\alpha \end{cases}, \quad (1)$$

where α is the rotation angle; u_m, v_m and w_m are the original wind velocity components measured. The directions of the velocity components are consistent with the orientation of the instrument during installation. This means that u_m is the east wind component, v_m is the north wind component, and w_m is the updraft component. The wind velocity components corrected by vertical rotation are u, v and w, respectively.

The turbulence data of 10 Hz are grouped by 30 min, and it can be considered that the turbulence field is approximately stable during the 30 min research period. Then, the coordinates in the horizontal directions are rotated, and the u-v plane is rotated around the w axis. Therefore, the u-w plane is in line with the average wind direction. This means u is toward the dominant flow direction within 30 min, and v is the lateral average flow direction. The rotation angle is β, and the wind velocity components after rotation are represented by subscript r. Therefore, the new wind velocity components are determined as follows:

$$\begin{cases} \beta = \arctan(\overline{v}/\overline{u}) \\ u_r = u\cos\beta + v\sin\beta \\ v_r = -u\sin\beta + v\cos\beta \\ w_r = w \end{cases}. \quad (2)$$

2.3 Energy spectrum calculation

According to the properties of motion and energy transport, the turbulence at various scales is divided into three specific subdomains (Kaimal and Finnigan, 1994): 1) the energy-containing subdomain corresponds to large-scale turbulence. The buoyancy and Reynolds stress generate turbulence kinetic energy. 2) The inertia subdomain corresponds to turbulence at a small scale. The turbulence kinetic energy dissipation of turbulence at all levels can be ignored. The turbulence kinetic energy can be transferred step by step to smaller scales. 3) The dissipative subdomain corresponds to the smallest-scale turbulence. Turbulence in this subdomain changes into internal energy under the action of fluid molecular viscosity.

Based on Kolmogorov's definition of locally homogeneous and isotropic turbulence (Kolmogorov, 1941a; Kolmogorov, 1941b), there is a high-wavenumber domain (high-frequency domain) when the Reynolds number is large, in which the turbulence is in a state of statistical equilibrium. The turbulence characteristics in this domain are only determined by the turbulence energy dissipation rate and molecular viscosity coefficient, satisfying the locally homogeneous and isotropic conditions. When the Reynolds number is larger, there is a subdomain determined only by the turbulence energy dissipation rate in the locally homogeneous and isotropic domain, namely, the inertia subdomain. According to this definition, the one-dimensional turbulence energy spectrum in the inertia subdomain can be obtained as follows:

$$S_{w,x}(k) \propto k^{-5/3}, \quad (3)$$

where S_w is the wavenumber spectrum, x is the three-dimensional wind velocity variable (u, v, w), and k is the wavenumber. This is the "$-5/3$ law," which is widely used in turbulence studies.

Based on Taylor's frozen turbulence hypothesis (Taylor, 1938), the observation results of turbulence at a fixed point in space are statistically equivalent to the observation of all points in space along the mean wind direction of the simultaneous segment. Thus, the wavenumber spectrum (S_w) can be equivalent to the frequency spectrum (S_f):

$$S_{f,x}(f) \propto f^{-5/3}, \quad (4)$$

where f is frequency, and $S_f\,\mathrm{d}f$ represents the contribution of turbulent components to turbulence kinetic energy between frequency $f \sim f + \mathrm{d}f$, namely, turbulence energy spectrum density. The frequency spectrum is normalized, and the normalized energy spectrum density is obtained as follows (Bian et al., 2002):

$$fS_{f,x}/\sigma_x^2 \propto f^{-2/3}, \quad (5)$$

where σ_x^2 is the variance in a three-dimensional time series of wind velocity variables.

In the calculation of the turbulence energy spectrum, the study period is usually taken as 30–60 min, during which sufficient data reflecting the characteristics of the statistical parameters of turbulence can be collected. At the same time, it is also believed that the statistical parameters of turbulence do not change with time during this study period, that is, the turbulence field is stable (Bian et al., 2002; Kaimal and Finnigan, 1994; Sheng et al., 2003). After preprocessing, the 10-Hz turbulence data are grouped every 30 min. Fast Fourier transform (FFT) is used to obtain the estimated energy spectrum of near-ground turbulence. However, the frequency spectrum directly obtained by FFT for the 30 min time series is generally rough and discrete in the high-frequency domain. For long time series data (data number $N >> 2^{10}$), the time series is usually decomposed into r uncrossed short time series.

Each frequency spectrum is calculated separately in each short time series where each length is N/r. Finally, the frequency spectra are averaged to obtain the estimation of the overall turbulence energy spectrum (Kaimal and Finnigan, 1994). N = 18000 and r = 10 are selected in this study. The Kolmogorov length is the turbulence scale of the dissipation subdomain when the wind velocity is at a magnitude of 10^0 m/s. That is, the corresponding turbulence scale and frequency magnitude are 10^{-3} m and 10^3 Hz, respectively (Kolmogorov, 1962). The energy spectrum of the dissipation subdomain cannot be obtained at the existing data sampling frequency. Therefore, the high-frequency spectrum corresponds to the turbulence inertia subdomain. Since we only care about the structure of the statistical energy spectrum in the inertial subdomain, we only need to calculate the high-frequency spectrum.

For stable turbulence with statistical parameters that do not change with time (t), the time correlation coefficient of a certain fixed point in space can be defined as follows:

$$R(t) = \frac{x'(t_0)x'(t_0+t)}{\sigma_x^2}, \tag{6}$$

where x' is the pulsation of the variable. The time correlation coefficient reflects the turbulence scale. If the space is dominated by large-scale turbulence, $x'(t_0)$ and $x'(t_0+t)$ are often in the same turbulence with a large correlation coefficient. If the space is dominated by small-scale turbulence, $x'(t_0)$ and $x'(t_0+t)$ are often in different turbulence with a small correlation coefficient. Taylor introduced the integral of the correlation coefficient to characterize the overall characteristic time in the turbulence field (Sheng et al., 2003), and to represent the expectation of life for all turbulence (Liao and Jiang, 2003):

$$T = \int_0^\infty R(t)\mathrm{d}t, \tag{7}$$

where T is the turbulence integral time scale. The turbulence integral length scale ($\sum$) based on Taylor's frozen turbulence hypothesis is determined as follows:

$$\sum = \int_0^\infty R(r)\mathrm{d}r = \overline{x}T. \tag{8}$$

In a similar way, the $\sum$ can characterize the overall characteristic length in the turbulence field, and represent the expectation of scale for all turbulence. According to the Eqs. (6)–(8), both of T and $\sum$ are based on the integral function of t. The magnitude of $\sum$ is proportional to t without taking into account any other variables. When the integral interval (t) is inconsistent, the magnitude of $\sum$ will have no significance.

3 Results and discussion

3.1 Dual polarization radar detects turbulence deformation

The reflectivity of turbulence (η) is given by Tatarski (1971) and Wilson et al. (1994):

$$\eta = 0.38\lambda^{-1/3}\cdot a^2\Delta n^2 L_0^{4/3}, \tag{9}$$

where λ is the radar wavelength, a is the dimensionless constant, n is the atmospheric refractive index, and L_0 is the outer scale of turbulence. The atmospheric refractive index turbulence structure constant is represented by $a^2\Delta n^2 L_0{}^{4/3}$. Under low elevation scanning condition, the radar beam is almost parallel to the ground. Thus the horizontally (or vertically) polarized wave is parallel (or perpendicular) to the ground without considering the elevation error. According to Eq. (9), the echo intensity of turbulence is positively correlated with the scale of turbulence, so Z_{DR} can be used as a criterion for the difference between horizontal and vertical scales of turbulence.

There was a squall line in the Yangtze and Huaihe River basins from July 30 to 31, 2014, which severely affected Henan, Anhui and Jiangsu. This squall line formed at 18:00 on July 30 (Beijing time, the same below), moved from north-west to south-east, and gradually weakened and dissipated after passing over Nanjing at 05:00 on the 31st. The NUIST CDP radar recorded this squall line. Abnormal Z_{DR} echoes are found in the gust front area of the squall line.

Figure 1 shows the gust front time series echoes of Z, V, Z_{DR} and ρ_{HV} in front of the squall line detected by NUIST CDP radar, corresponding to three consecutive moments at 00:37, 00:44 and 00:51, respectively, on July 31, 2014. The elevation is 1.45°, and the distance circle represents 30 km. The gust front is formed in the nonprecipitation area approximately 10–15 km in front of the squall line, and the echo is slightly stronger than the surrounding echo (dotted line in Fig. 1). The echo shows an obvious velocity convergence line in V, after which it is a west wind with the maximum and ambiguous Doppler radial velocity close to 22 m/s. The ρ_{HV} of the gust front is stable at 0.70, which is different from other nonprecipitation clutter. The Z_{DR} of the gust front decreases first and then increases from north to south, and a negative Z_{DR} appears before and after the gust front. This phenomenon only occurs at lower elevations (below 3°), which is in line with the characteristics of the gust front echo. The discussion of turbulence deformation shows that the shape of turbulence is changed due to the influence of the ambient wind (Huang et al., 2018). The turbulence is affected by a strong west wind in the gust front, which is arranged in a horizontal bar shape in the east–west direction. The long axes of the deforming turbulence in the 330° direction

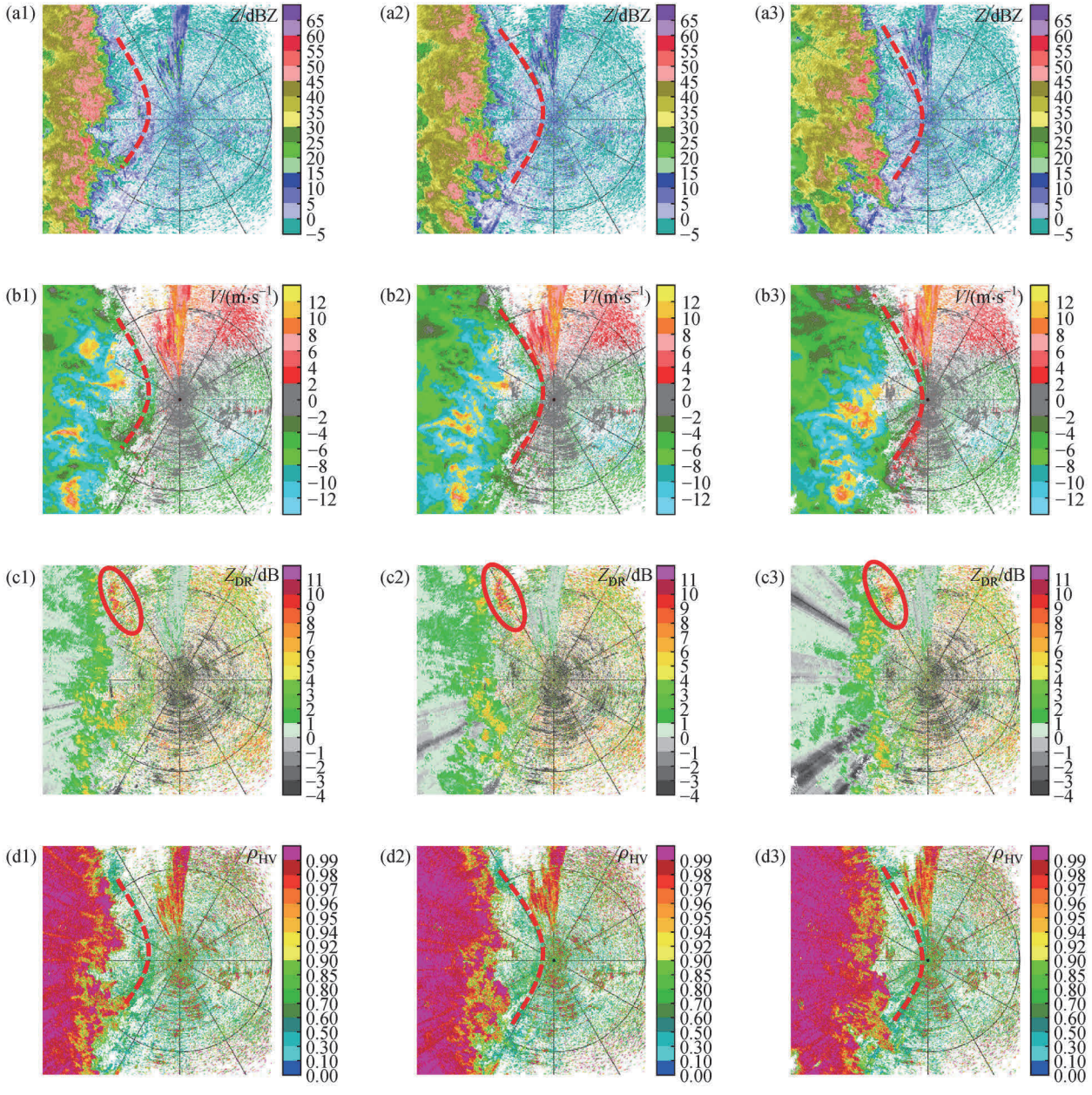

Fig. 1 Squall line echoes taken at 1.45° for (a) Z, (b) V, (c) Z_{DR} and (d) ρ_{HV} at 00:37, 00:44 and 00:51, respectively, on July 31, 2014. The distance circle and dotted line in (a), (b) and (d) represent 30 km and the location of gust front, respectively.

project completely on the radar cross section, which shows Z_{DR} anomalies of 8–9 dB. In contrast, it does not project in the 270° direction, so Z_{DR} decreases. Meanwhile, warm air before the gust front is forced to rise, and the cold air after the gust front drops rapidly, which is different from the general horizontal moving atmosphere. In theory, it is speculated that the turbulence scale should be the maximum in the vertical direction, and the corresponding Z_{DR} values at the front and back of the gust front are negative, which is consistent with the observation.

3.2 Energy spectrum analysis of turbulence deformation

The turbulence data obtained from the three-dimensional ultrasonic anemometer are used to discuss the shape parameters of turbulence in detail. The data are averaged every 30 min to obtain the average wind direction and speed in the approximately stable turbulence field, as shown in Fig. 2. The wind directions at the observation site changed from south to east and then south-east on March 13, 2017. The surface wind speed is relatively low at

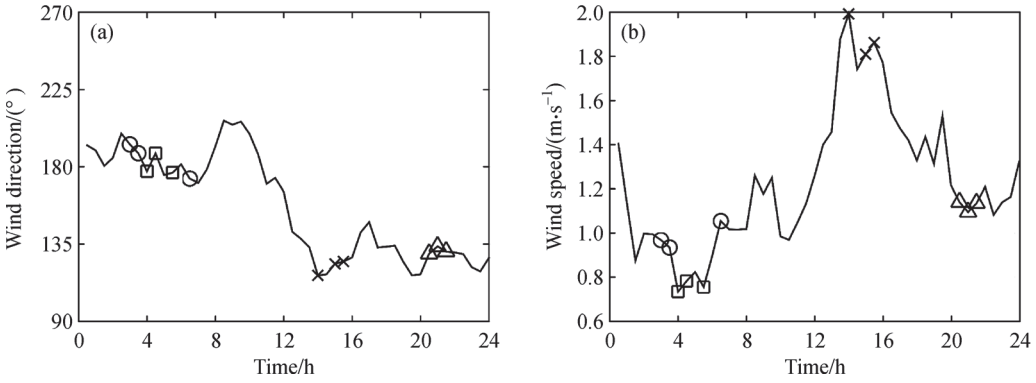

Fig. 2 Average wind direction and speed in 30 min in Zhanjiang, Guangdong Province on March 13, 2017. The circles represent south winds with high speeds, crosses represent quasi-east winds with higher speeds, squares represent south winds with low speeds, and triangles represent south-east winds with high speeds.

04:00, and the average speed is below 0.8 m/s. The surface wind speed is at a maximum of approximately 2.0 m/s at 14:00. Several classical wind directions and speeds are selected for turbulence energy spectrum analysis. The selected time period is divided into 4 cases and marked with different symbols: I) south winds with high speeds (circle); II) quasi-east winds with higher speeds (cross); III) south winds with low speeds (square); and IV) south-east winds with high speeds (triangle). Three groups of energy spectra are analyzed for each case.

To highlight the relationship between wind direction and turbulence orientation, the turbulence data used in 3.1–3.4 are only corrected by the coordinate rotation in the vertical direction, while the turbulence data used in 3.5 are corrected by the DR in the vertical and horizontal directions.

3.2.1 South winds with high speeds (case I)

By analyzing the statistical characteristics of the turbulence energy spectrum during 02:30–03:00, 03:00–03:30 and 06:00–06:30 on March 13, 2017, the average wind direction during this period is south, with an average direction of 184.51° and an average speed of 0.99 m/s.

The energy spectral density of the east wind component (u), the north wind component (v) and the updraft component (w) are shown in Fig. 3(a). The horizontal axis is the normalized frequency, and the vertical axis is the normalized energy spectral density. The dashed line in Fig. 3(a) is $10^{-2/3}$. The slope of the inertia subdomain spectra conforms to $-2/3$. The normalized frequency spectra come from the wavenumber spectra based on Taylor's frozen turbulence hypothesis. Therefore, the

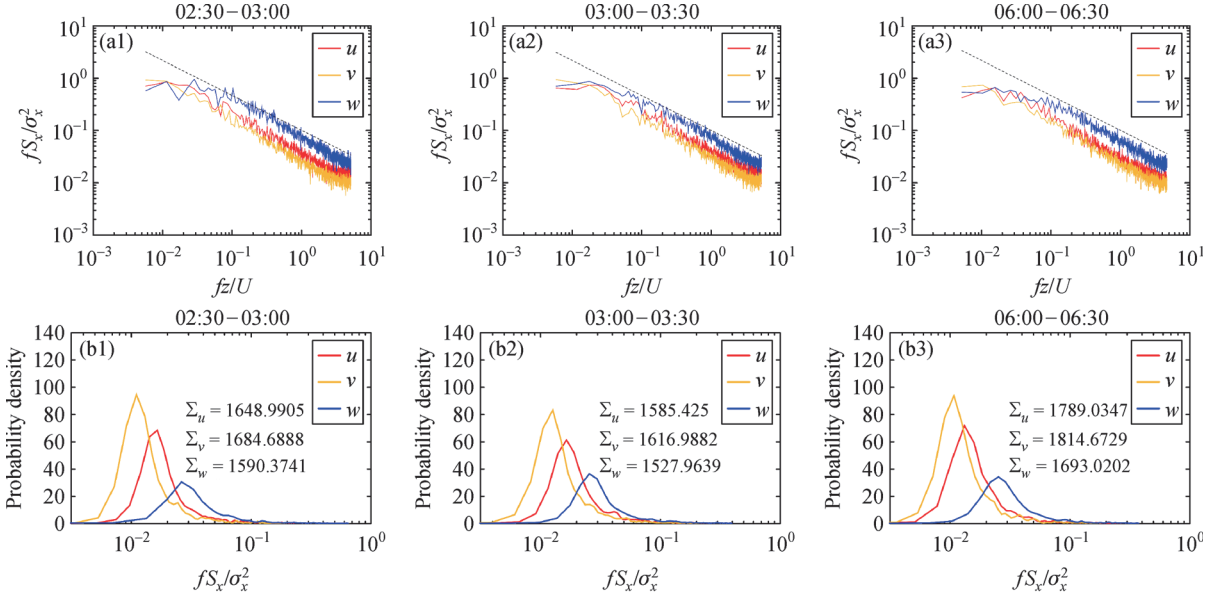

Fig. 3 (a) Normalized turbulence energy spectral density and (b) its probability density in case I, where u represents the east wind component, v represents the north wind component, and w represents the updraft component. Σ_u, Σ_v and Σ_w represent the turbulence integral length scale in the u, v and w directions, respectively. The dashed line in (a) is $10^{-2/3}$.

high-frequency domain corresponds to the high-wavenumber and small-scale domain. In the high-frequency domain, $S_{f,v} < S_{f,u} < S_{f,w}$, namely, for the same turbulence energy spectral density, there is a low frequency in the v direction, a high frequency in the u direction, and a higher frequency in the w direction. Most of the previous observations show that $S_{f,u} < S_{f,v} < S_{f,w}$ in the atmospheric boundary layer under the condition of flat terrain (Kaimal and Finnigan, 1994; Wu et al., 2011; Wyngaard, 1990). The reason is that u direction is generally defined as the average flow direction. To discuss the deformation of turbulence influenced by environmental wind in this paper, the east direction is defined as u direction. Only coordinate rotation correction in the vertical direction is carried out in Fig. 3, so the energy spectrum distribution phenomenon is different from that in the past. Deformation of turbulence occurs under the influence of the south wind. The three-dimensional nonspherical characteristics of the turbulence scale are larger in the v direction, large in the u direction, and small in the w direction.

The probability density of the energy spectrum density in the corresponding period is shown in Fig. 3(b), which reveals the contribution of the three wind components to the turbulence energy spectrum density more intuitively. The peak value of the turbulence energy spectrum density in the v direction is approximately $10^{-2.0}$, the peak value of the probability density is the largest, and the spectrum shape is the narrowest of the three components. The peak values of the turbulence energy spectrum density in the u direction and w direction are approximately $10^{-1.9}$ and $10^{-1.8}$, respectively, and the probability density broadening in the w direction is the most obvious. Generally, because atmospheric motion is mainly in the horizontal (u-v) direction, the vertical motion speed and uniformity are much lower than the horizontal motion. When turbulence flows through a horizontal plane, the momentum will exchange between this planes, making the average speed homogeneous. The upper fluid exerts a turbulent shear stress on the lower fluid through this plane and accelerates the lower fluid. As a result, the turbulence flux in the w direction of the atmosphere is much larger than that in the u-v direction, and the velocity pulsation in the w direction of the atmosphere is significantly higher than that in the u-v direction. Turbulence will deform under the influence of a strong south wind. Similar to $\sum$, the turbulence integral length scale in the u direction ($\sum_u$), v direction ($\sum_v$) and w direction ($\sum_w$) represents the expectation of scales for all turbulence in the u, v and w direction, respectively. The relationships of turbulence three-dimensional integral length scale are $\sum_v > \sum_u > \sum_w$, corresponding to a larger turbulence scale in the v direction, a large scale in u direction, and a small scale in w direction.

3.2.2 Quasi-east winds with higher speeds (case II)

There is no obvious east wind on this day, so the period of a nearly east wind is used to replace the east wind turbulence field. By analyzing the statistical characteristics of the turbulence energy spectrum during 13:30–14:00, 14:30–15:00 and 15:00–15:30 on March 13, 2017, the average wind direction during this period is 121.55°, and the average speed is 1.89 m/s.

The wind speed between 13:30 and 14:00 is the maximum on this day, with a speed of 1.99 m/s and a direction of 116.55°, which is closest to the east wind turbulence field. At this time, the turbulence statistical

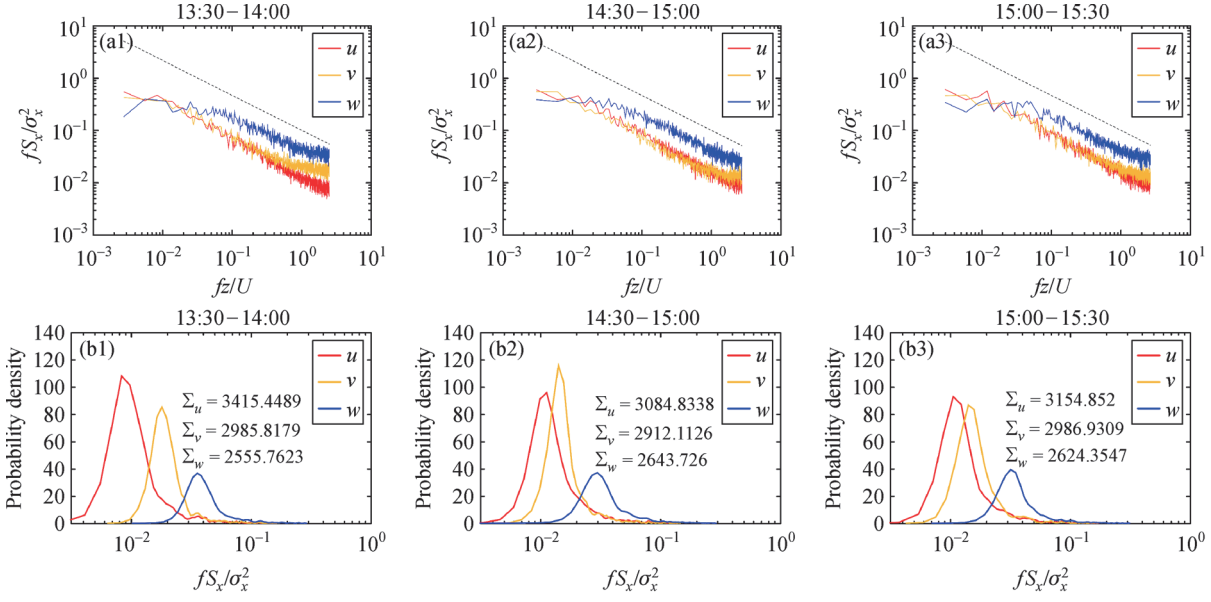

Fig. 4 Same as Fig. 3, but in case II.

characteristics are shown in Fig. 4. The deformation, location and orientation of turbulence are obviously changed compared with those when the south wind is dominant. The turbulence energy spectrum density relationships in three directions are $S_{f,u} < S_{f,v} < S_{f,w}$, with a more obvious difference among them. Moreover, compared with case I, the spectral lines of energy spectral density exhibit overall displacements toward the large-scale and low energy spectral density domain, indicating that the turbulence scale becomes larger when the environmental wind speed increases. The probability density of the turbulence energy spectral density is more significantly different in the statistical characteristics of turbulence in the orthogonal directions. The peak probability density in the u direction is obviously larger than that in the other two directions, and the probability density spectrum in the u direction is narrower under the influence of a high wind speed. The relationships of turbulence integral length scale in three directions are $\sum_u > \sum_v > \sum_w$ with the maximum value of $\sum_u = 3415$ in the period of the highest wind speed, corresponding to a larger turbulence scale in the u direction, a large scale in v direction, and a small scale in w direction under the influence of a quasi-east wind with a higher speed. The nonspherical deformation characteristics of turbulence are more obvious.

3.2.3 South winds with low speeds (case III)

By analyzing the statistical characteristics of the turbulence energy spectrum during 03:30–04:00, 04:00–04:30 and 05:00–05:30 on March 13, 2017, the average wind direction during this period is 180.42°, which is consistent with case I, but the average speed is 0.76 m/s.

Compared with cases I and II, the spectral lines of energy spectral density display displacements as a whole toward the small-scale and high energy spectral density domain in Fig. 5(a), indicating a smaller turbulence scale. The statistical characteristics in the u and v directions are similar, with a performance for $S_{f,u} \approx S_{f,v}$ in the turbulence energy spectral density. The spectra in the u and v directions basically coincide in Fig. 5(b) but are wider than cases I and II with high wind speeds. The turbulence integral length scale is $\sum_u \approx \sum_v > \sum_w$, which corresponds to the isotropic characteristics in the u-v directions but is deformed in the w direction. The nonspherical turbulence has similar scales in the u-v directions and the smallest scale in the w direction.

3.2.4 South-east winds with high speeds (case IV)

By analyzing the statistical characteristics of the turbulence energy spectrum during 20:00–20:30, 20:30–21:00 and 21:00–21:30 on March 13, 2017, the average wind direction during this period is south-east, with an average direction of 131.07 ° and an average speed of 1.12 m/s.

As shown in Fig. 6, compared with case III, the spectral lines of the energy spectral density exhibit overall displacements toward the large-scale and low energy spectral density domain under the influence of a high wind speed, and the turbulence integral length scale increases obviously. The rest of the characteristics are very similar in both cases III and IV. The direct observation results show that the turbulence is also isotropic in the u-v directions. However, the wind direction is south-east, and the directly measured three-dimensional characteristics of turbulence

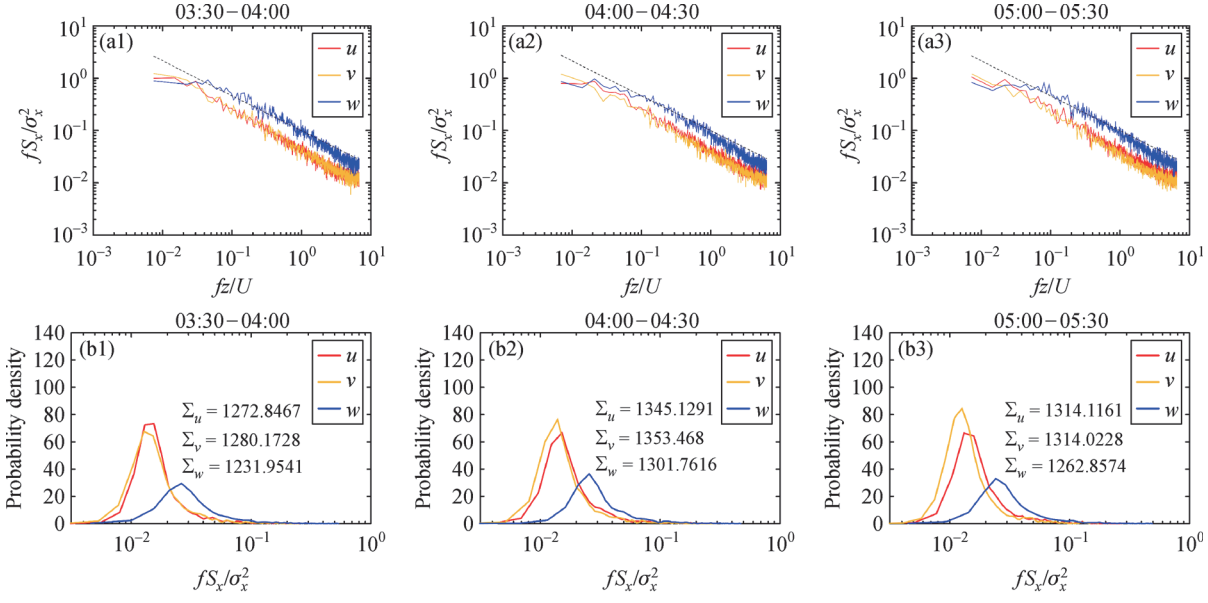

Fig. 5 Same as Fig. 3, but in case III.

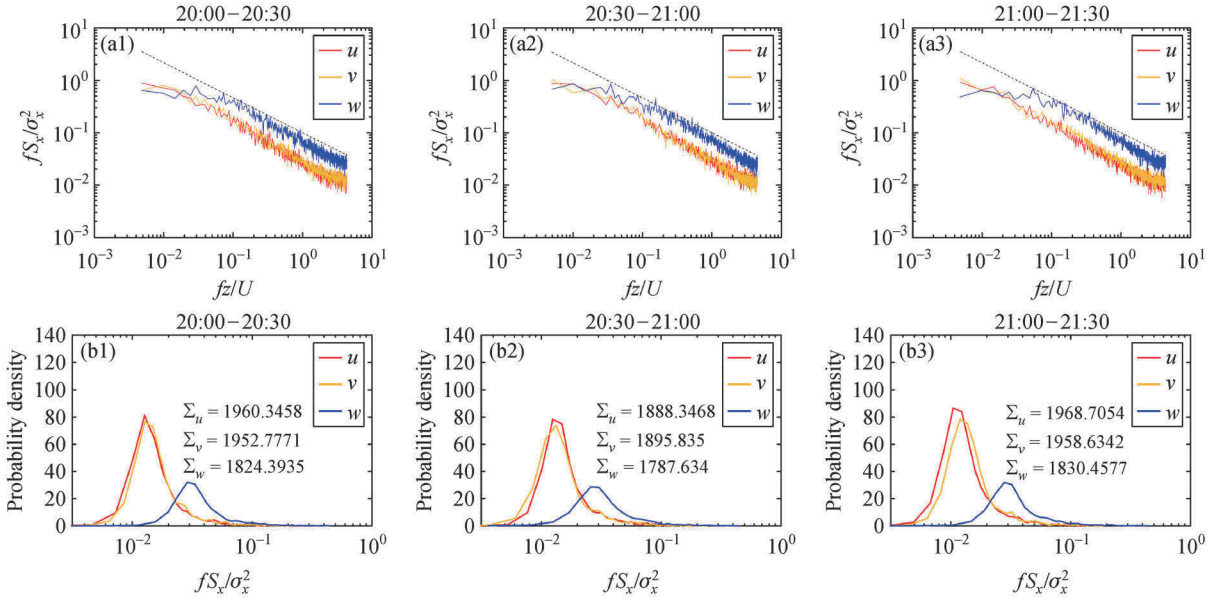

Fig. 6 Same as Fig. 3, but in case IV.

are orthogonally projected in the east, north and vertical directions. The projected results misrepresent the actual characteristics of the turbulence scale. Therefore, the observation coordinates are rotated in the horizontal direction to eliminate the misleading orthogonal projection.

3.3 Scale parameterization and evaluation of turbulence deformation

To eliminate the misleading orthogonal projection, coordinate rotation corrections are carried out for cases III and IV in the horizontal direction using Eq. (2). The *u*-*v* plane is rotated around the *w* axis. Therefore, the *u*-*w* plane is in line with the average wind direction, which means that *u* is toward the dominant flow direction within 30 min, and *v* is the lateral average flow direction. The wind velocity components after rotation are represented by subscript *r*. After the rotation, u_r represents the south wind component, and v_r represents the east wind component in case III. However, u_r represents the south-east wind component, and v_r represents the north-east wind component in case IV. The w_r remains the same as *w*.

The probability density of the normalized turbulence energy spectrum density for cases III and IV in each period after the coordinate rotation is shown in Figs. 7(a) and 7(b), respectively. In case III, the turbulence still exhibits horizontal isotropic characteristics after coordinate rotation, which confirms that the turbulence deformation is not obvious due to the low horizontal wind speed. However, in case IV, the turbulence scale is the largest along the dominant wind direction, and the anisotropic characteristics are obvious, which conforms to the relationship between turbulence deformation and environmental wind. Under the condition of weak horizontal wind, the statistical parameters of turbulence in *u* and *v* direction are similar, which are obviously different from *w* direction after coordinate double rotation corrections. A similar phenomenon was found in the study of Frank et al. (2013) and Wu et al. (2011). The statistical parameter characteristics in *u* direction correspond to larger scale turbulence with the increase of horizontal wind speed.

The overall characteristic length of the turbulence field can be expressed by the turbulence integral length scale ($\sum$). There are significant positive correlations with $\sum$ and wind speed in cases I–IV. After the DR correction by Eqs. (1) and (2), each $\sum$ during 30 min is fitted with the horizontal wind speed by a power function that obtains the best fitting effect, and the goodness of fit (*GF*) is above 0.99 in the *u*, *v* and *w* directions, as shown in Fig. 8. The fitting equations in each direction are listed below:

$$\begin{cases} \sum_u = 1.890 \times 10^3 x^{0.8816} - 1.612 \times 10^2 \\ \sum_v = 2.663 \times 10^3 x^{0.6290} - 9.432 \times 10^2 \\ \sum_w = 2.377 \times 10^4 x^{0.06242} - 2.212 \times 10^4 \end{cases}. \quad (10)$$

The relationship between the radial velocity and the turbulence scale in the gust front area, discussed in section 3.1, is obtained by using the parametric model of the turbulence scale and the environmental wind speed, as shown in Fig. 9. The maximum Doppler radial velocity is close to 22 m/s in the front, corresponding to three-dimensional turbulence integral length scales of $\sum_u = 2.868 \times 10^4$, $\sum_v = 1.766 \times 10^4$ and $\sum_w = 6.707 \times 10^3$.

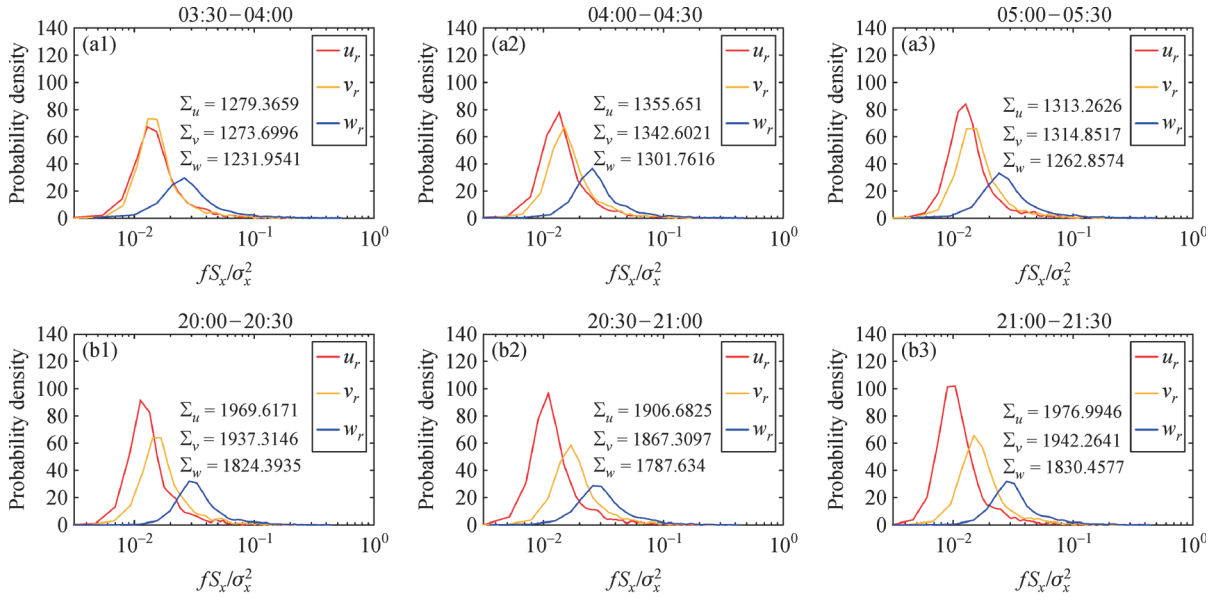

Fig. 7 Probability density of the normalized turbulence energy spectrum density after horizontal coordinate rotation in (a) case III and (b) case IV, where u_r represents the component of the dominant flow direction within 30 min, v_r represents the component of the lateral average flow direction, and w_r represents the updraft component.

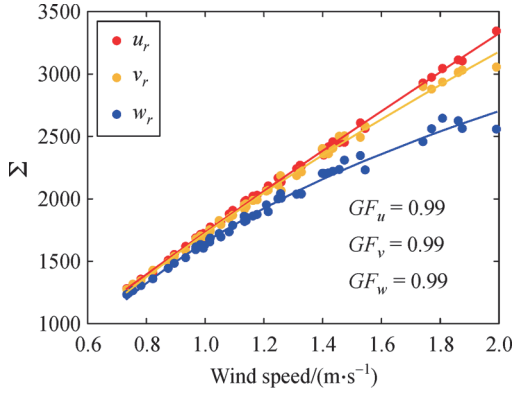

Fig. 8 A parametric model of turbulence integral length scale (Σ) and wind speed.

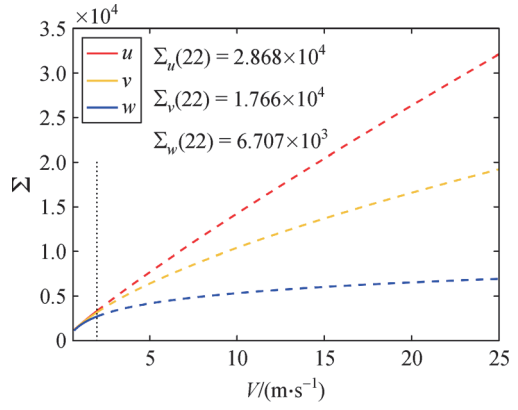

Fig. 9 The relationship between radial velocity and turbulence scale in the gust front by the parametric model of turbulence integral length scale and wind speed.

All of $\sum u$, $\sum v$ and $\sum w$ are based on the integral function of consistent t. Therefore, the ratio of $\sum u$ and $\sum w$ equals to the ratio of turbulence actual scale in the u direction (L_u) and in the w direction (L_w). The ratio of the horizontal and vertical scales of turbulence deformation projected on the radar cross section is $L_u/L_w = \sum u/\sum w \approx 4.3$ when the long axis of turbulence is orthogonal with the radar detection direction. According to the definition of Z_{DR} and Eq. (9), it can be estimated that the ratio of horizontal and vertical scales of the corresponding turbulence is $L_u/L_w \approx 4.0$–4.7 when Z_{DR} reaches 8–9 dB. The shape of the turbulence calculated from the radar detection results is consistent with the results of the parametric model.

4 Conclusions

1) Based on the turbulence energy spectrum analysis, the turbulence deformation exist. In general, the atmosphere is dominated by horizontal motion, and the horizontal scale of turbulence is generally larger than the vertical scale. The turbulence is nearly isotropic in the horizontal direction, presenting a flat ellipsoid with the vertical orientation of the rotation axis when there is no horizontal wind or the horizontal velocity is small. When horizontal wind exists, the turbulence scale increases along the dominant wind direction.

2) The overall characteristic length of the turbulence field can be expressed by the turbulence integral length

scale. It is positively correlated with the wind speed. The power function is used to fit the relationships of turbulence integral length scale and horizontal wind speed, which obtains the best fitting effect, and the *GF* is above 0.99 in each direction. The maximum Doppler radial velocity is close to 22 m/s in the gust front located in front of the squall line, which the ratio of scales in the dominant wind and the vertical direction of deforming turbulence (L_u/L_w) is around 4.3.

3) The gust front is a narrow linear echo in Z that is affected by strong turbulence. It is an obvious velocity convergence line in V and approximately 0.70 in ρ_{HV}. The results reveal the mechanism of abnormal Z_{DR} echo caused by turbulence deformation. The turbulence deformation can cause 8–9 dB Z_{DR} anomalies in the dual polarization radar echo in the nonprecipitation area with high horizontal wind speed, which corresponds to a turbulence deformation horizontal and vertical scale ratio of $L_u/L_w \approx 4.0$–4.7. The variation in Z_{DR} depends on the turbulence shape, orientation and the relative position between turbulence and radar. The shape of turbulence derived from the radar detection results is consistent with that of the parametric model, which can provide a parametric scheme for turbulence research.

Acknowledgements Prof. Lv Jingjing, in School of Atmospheric Physics, Nanjing University of Information Science & Technology, assisted in field observation and data acquisition. This work was supported by the National Natural Science Foundation of China (Grant No. 41675029), the Natural Science Foundation of Shandong Province (Nos. ZR2020MD052 and ZR2020MD053), and the Shanghai Aerospace Science and Technology Innovation Fund Project (No. SAST2019-097).

References

Bian J, Qiao J, Lv D (2002). Reanalysis of the turbulent spectra in the atmospheric surface layer. Chin J Atmos Sci, 26(4): 474–480

Bragg W L (1913). The structure of some crystals as indicated by their diffraction of X-rays. Proc R Soc Lond, 89(610): 248–277

Businger J A, Wyngaard J C, Izumi Y, Bradley E F (1971). Flux-profile relationships in the atmospheric surface layer. J Atmos Sci, 28(2): 181–189

Doviak R J, Zrnic D S, Schotland R M (1994). Doppler Radar and weather observations. Appl Opt, 33(21): 4531

Du M, Liu L, Hu Z, Yu R (2012). Quality control of differential propagation phase shift for dual linear polarization radar. Journal of Applied Meteorological Science, 23(6): 710–720

Frank J M, Massman W J, Ewers B E (2013). Underestimates of sensible heat flux due to vertical velocity measurement errors in non-orthogonal sonic anemometers. Agric Meteorol, 171–172: 72–81

Guo J, Bian L, Dai Y (2007). Measured CO_2 concentration and flux at 16 m height during corn growing period on the North China Plain. Chin J Atmos Sci, 31(4): 695–707

Hu Z, Liu L, Chu R, Jin R (2008). Comparison of different attenuation correction methods and their effects on estimated rainfall using X-band dual linear polarimetric radar. Acta Meteorol Sin, 66(2): 251–261

Huang Q, Wei M, Hu H, Abro M I (2018). Analysis of atmospheric wind, temperature and humidity structure and dual-polarization radar parameters of clear air echo. Meteorological monthly, 44(4): 526–537

Kaimal J C, Finnigan J J (1994). Atmospheric Boundary Layer Flows: Their Structure and Measurement. New York: Oxford University Press

Kanda M, Inagaki A, Letzel M O, Raasch S, Watanabe T (2004). LES study of the energy imbalance problem with eddy covariance fluxes. Boundary-Layer Meteorol, 110(3): 381–404

Knight C A, Miller L J (1993). First radar echoes from cumulus clouds. Bull Am Meteorol Soc, 74(2): 179–188

Kolmogorov A N (1962). A refinement of previous hypotheses concerning the local structure of turbulence in a viscous incompressible fluid at high reynolds number. J Fluid Mech, 13(1): 82–85

Kolmogorov A N (1941a). Energy dissipation in locally isotropic turbulence. Proceedings of the Royal Society a Mathematical Physical & Engineering Sciences, 434(1890): 16–18

Kolmogorov A N (1941b). The local structure of turbulence in incompressible viscous fluid for very large reynolds numbers. Sov Phys Usp, 30(4): 301–305

Liao S, Jiang D (2003). Method to extract turbulent characteristic parameters based on wavelet analysis. Journal of Combustion Science and Technology, 9(1): 21–28

Ma Z (1986). Information and Principle of Weather Radar Echo. Beijing: Science Press (in Chinese)

Melnikov V M, Doviak R J, Zrnic D S, Stensrud D J (2013). Structures of bragg scatter observed with the polarimetric WSR-88D. J Atmos Ocean Technol, 30(7): 1253–1258

Monin A S, Obukhov A M (1954). Basic laws of turbulent mixing in the surface layer of the atmosphere. Trudy Geofizicheskogo Instituta. Akademiya Nauk SSSR, 24(151): 163–187

Richardson L M, Cunningham J G, Zittel W D, Lee R R, Ice R L, Melnikov V M, Hoban N P, Gebauer J (2017). Bragg scatter detection by the WSR-88D. Part I: algorithm development. J Atmos Ocean Technol, 34(3): 465–478

Sheng P, Mao J, Li J, Zhang A, Sang J, Pan N (2003). Atmospheric Physics. Beijing: Peking University Press (in Chinese)

Tang Y (2014). The scattering mechanism and analysis of clear-air echo. Dissertation for Master's Degree. Nanjing: Nanjing University of Information Science & Technology (in Chinese)

Tatarski V I (1971). The effects of the turbulent atmosphere on wave propagation. National Technical Information, TT-68–50464

Tatarski V I, Silverman R A, Chako N (1961). Wave propagation in a turbulent medium. Phys Today, 14(12): 46–51

Taylor G I (1938). The Spectrum of turbulence. Proceedings of the Royal Society of London A: Mathematical, Physical and Engineering Sciences, 919: 476–490

Vickers D, Mahrt L (1997). Quality control and flux sampling problems for tower and aircraft data. J Atmos Ocean Technol, 14(3): 512–526

Wang J, Wang W, Ao Y, Sun F, Shu G (2007). Turbulence flux measurements under complicated conditions. Advances in Earth Science, 22(8): 791–797 (in Chinese)

Wang J, Wang W, Liu S, Ma M, Li X (2009). The problems of surface energy balance closure—an overview and case study. Advances in Earth Science, 24(7): 705–713 (in Chinese)

Wang Y, Chandrasekar V (2009). Algorithm for estimation of the specific differential phase. J Atmos Ocean Technol, 26(12): 2565–2578

Wilczak J M, Oncley S P, Stage S A (2001). Sonic anemometer tilt correction algorithms. Boundary-Layer Meteorol, 99(1): 127–150

Wilson J W, Weckwerth T M, Vivekanandan J, Wakimoto R M, Russell R W (1994). Boundary layer clear-air radar echoes: origin of echoes and accuracy of derived winds. J Atmos Ocean Technol, 11(5): 1184–1206

Wu B, Zhang H, Wang Z, Zhu H, Xie Y (2011). Study on turbulent structures and energy transfer during an advective fog period. Acta Scientiarum Naturalium Universitatis Pekinensis, 47(2): 295–301

Wyngaard J C (1990). Scalar fluxes in the planetary boundary layer—theory, modeling and measurement. Boundary-Layer Meteorol, 50(1–4): 49–75

Xu Z, Liu S, Gong L, Wang J, Li X (2008). A study on the data processing and quality assessment of the eddy covariance system. Advances in Earth Science, 23(4): 357–370

Yao X (2016). Data quality control and echo characteristics analysis of NUIST-C Band dual linear polarimetric doppler radar. Dissertation for Master's Degree. Nanjing: Nanjing University of Information Science & Technology (in Chinese)